Electronic structure of the SiN_x/TiN interface: A model system for superhard nanocomposites

Jörg Patscheider,[1,2,*] Niklas Hellgren,[2,3] Richard T. Haasch,[2] Ivan Petrov,[2] and J. E. Greene[2]

[1]*EMPA, Laboratory for Nanoscale Materials Science, Überlandstrasse 129 CH-8600 Dübendorf, Switzerland*

[2]*Department of Materials Science and Frederick Seitz Materials Research Laboratory University of Illinois, 104 S. Goodwin Avenue, Urbana, Illinois 61801, USA*

[3]*Messiah College, Department of Mathematical Sciences, P.O. Box 3041, One College Ave., Grantham, Pennsylvania 17027, USA*

(Received 9 November 2010; published 31 March 2011)

Nanostructured materials such as nanocomposites and nanolaminates—subjects of intense interest in modern materials research—are defined by internal interfaces, the nature of which is generally unknown. Nevertheless, the interfaces often determine the bulk properties. An example of this is superhard nanocomposites with hardness approaching that of diamond. TiN/Si_3N_4 nanocomposites (TiN nanocrystals encapsulated in a fully percolated SiN_x tissue phase) and nanolaminates, in particular, have attracted much attention as model systems for the synthesis of such superhard materials. Here, we use *in situ* angle-resolved x-ray photoelectron spectroscopy to probe the electronic structure of Si_3N_4/TiN(001), Si/TiN(001), and Ti/TiN(001) bilayer interfaces, in which 4-ML-thick overlayers are grown in an ultrahigh vacuum system by reactive magnetron sputter deposition onto epitaxial TiN layers on MgO(001). The thickness of the Si_3N_4, Si, and Ti overlayers is chosen to be thin enough to insure sufficient electron transparency to probe the interfaces, while being close to values reported in typical nanocomposites and nanolaminates. The results show that these overlayer/TiN(001) interfaces have distinctly different bonding characteristics. Si_3N_4 exhibits interface polarization through the formation of an interlayer, in which the N concentration is enhanced at higher substrate bias values during Si_3N_4 deposition. The increased number of Ti-N bonds at the interface, together with the resulting polarization, strengthens interfacial bonding. In contrast, overlayers of Si and, even more so, metallic Ti weaken the interface by minimizing the valence band energy difference between the two phases. A model is proposed that provides a semiquantitative explanation of the interfacial bond strength in nitrogen-saturated and nitrogen-deficient Ti-Si-N nanocomposites.

DOI: 10.1103/PhysRevB.83.125124 PACS number(s): 79.60.Dp, 68.35.−p, 73.20.−r, 81.05.Je

I. INTRODUCTION

An intense area of current research is the synthesis of superhard (hardness H $\geqslant$ 40 GPa[1]) nanocomposites for use as wear-resistant coatings on tools and mechanical components as well as scratch-resistant thin films on optics. The nanocomposites are composed of nanocrystallites ($\leqslant$10 nm in size) of transition metal nitrides, carbides, or borides encapsulated by a few monolayers (ML) of a covalent interfacial layer (e.g., Si_3N_4, BN, CN_x, or C). Due to the small dimensions across the nanograins, nucleation and glide of dislocations is impeded, while the high cohesive strength of the thin intergranular tissue phase inhibits grain-boundary sliding.[2] Together these effects provide a qualitative explanation for the observed superhardness of the nanocomposites. The pseudobinary Si_3N_4-TiN system, which presently serves as an archetype in the quest for superhard nanocomposite materials,[1,3–8] exhibits strong phase segregation (Si_3N_4 and TiN have essentially no solid solubility[9]), a prerequisite for self-organized nanocomposite formation during vapor phase deposition. The growth of superhard SiN_x/TiN nanolaminates has also been reported with mechanical properties similar to isotropic TiN/Si_3N_4 nanocomposites.[10]

Unambiguous identification of the deformation mechanism of nanocomposites is hampered by the small dimensions of the phases involved, 5 to 10 nm for the grain size and 1 to 2 ML, on average, for the tissue phase. Although there is a paucity of detailed experimental results on failure mechanisms in ceramic nanocomposites, the most likely pathway for the deformation of nanocrystalline materials under load is grain boundary sliding.[1] Using nanocrystalline metals with amorphous grain boundaries for comparison, molecular dynamics (MD) calculations show a transition in the primary deformation mechanism from dislocation-dominated material flow to grain boundary sliding at crystallite sizes below 10–15 nm.[11] For nanocrystalline Ni, with grain sizes <15 nm, the grain interiors are virtually free from point defects that can act as sources for dislocations and slip.[12] Such grains do not deform plastically; rather, they slide against each other to accommodate macroscopic strain imposed during mechanical deformation. From these results, it seems clear that the nature of the tissue phase and the crystallite/tissue-phase interface is fundamental to defining the macroscopic properties of nanocomposites such as TiN/Si_3N_4 for which extraordinary mechanical properties including high hardness and fracture resistance have been reported.[13,14]

The degree of Si nitridation in TiN/SiN_x ($x \leqslant 1.33$) nanocomposite layers deposited by magnetron sputtering influences the hardness of these materials. Films deposited under conditions of insufficient nitridation exhibit little or no hardness enhancement,[4,15] demonstrating that a sufficiently high N concentration is necessary for high hardness. Intense discharges provide such conditions for efficient N incorporation and are essential for optimal interfacial SiN_x/TiN bonding in superhard nanocomposites.[2,4]

The chemical nature of the SiN_x/TiN interface and the SiN_x tissue phase can, in principle, be determined by angle-resolved photoelectron spectroscopy (AR-XPS). However, the extreme curvature of such interfaces in nanocomposites presents a severe challenge to the use of standard analytical methods. Electron energy loss spectroscopy (EELS), in combination

with high resolution transmission electron microscopy (HRTEM), for example, is capable of probing chemical changes in the subnanometer range; however, probing the interface between two crystallites requires that they are imaged without superposition of additional grains. This, in turn, means that the specimen thickness should be of the order of the crystallite size (i.e., less than 10 nm). Apart from the problems with the mechanical stability of such thin lamellae, their preparation by focused ion beam (FIB) or ion milling typically results in 5 to 10 nm of the surface region being amorphized. Hence, analysis free from artifacts is extremely difficult.

Here, we approach the problem of isolating and probing SiN_x/TiN interface chemistry by preparing planar interfaces in the form of Si_3N_4/TiN(001), Si/TiN(001), and Ti/TiN(001) bilayers starting with well-defined TiN(001) surfaces and depositing 4-ML thick Si_3N_4, Si, and Ti overlayers. To minimize contamination effects, film growth experiments are performed in an ultrahigh vacuum (UHV) and analyzed *in situ* using AR-XPS. The Si_3N_4 overlayers are grown at room temperature by magnetron sputtering in Ar/N_2 mixtures (total pressure P = 0.5 Pa (3.75 mTorr), N_2 partial pressure $P_{N2} = 0.25$ Pa (1.88 mTorr)), conditions known to provide fully nitrided amorphous Si_3N_4.[16,17]

Lower hardness values are obtained from TiN/SiN_x nanocomposites with incomplete nitridation.[4,15] The nitrogen deficiency leads to $SiN_{1.33-x}$ as can be deduced from the Si 2p core level peak in XPS. As limiting cases, we therefore consider, in addition to Si_3N_4/TiN interfaces, Si/TiN, and Ti/TiN. This completes the range of interfaces from insulating to semiconducting to metallic overlayers on TiN.

II. EXPERIMENTAL PROCEDURES

Epitaxial, 250-nm thick, layers of TiN are grown on MgO(001) via magnetically unbalanced magnetron sputtering, following the procedure described in detail,[18] from a solid 99.9999% pure Ti target in a multichamber UHV system [base pressure $\sim 1 \cdot 10^{-7}$ Pa ($<10^{-9}$ Torr)]. The 50-mm diameter Ti magnetron target is mounted along the outer wall of a cylindrical deposition chamber and separated by 40 cm from the second target position to inhibit cross-contamination between the targets. The substrates are cleaned in successive rinses in ultrasonic baths of trichloroethane, acetone, methanol, and deionized water, blown dry with dry N_2, inserted into the UHV system and heated to 800 °C for one hour, giving rise to well-ordered MgO(001)1 × 1 surfaces as determined by low-energy electron diffraction analyses.[19] TiN deposition is carried out in mixed 50:50 Ar:N_2 atmospheres at a total pressure of 0.5 Pa (3.75 mTorr).

The TiN(001) layers are grown at 600 °C, a target power of 100 W, a cathode potential of 385 V, and a floating potential of −7 V, resulting in a deposition rate of 0.4 Å/min, conditions known to lead to high quality stoichiometric single crystals.[18] The freshly grown TiN(001) surfaces serve as lower layers of interfaces formed by the overgrowth of 4 ML of Si_3N_4, Si, or Ti, without breaking vacuum, in separate experiments. The electronic grade 99.9999% pure Si target is sputtered at 20 W (374 V) in pure Ar at 0.5 Pa (3.75 mTorr) to deposit Si layers at room temperature, and with a target voltage of 350 V in 50:50 Ar:N_2 to deposit Si_3N_4. The Si_3N_4 layers are found, by *ex situ* Rutherford backscattering spectroscopy (RBS) analysis to be stoichiometric (N/Si = 1.32) with an overlayer of 2.5 ML SiO_2 due to air exposure between deposition and analysis. Si_3N_4 layers are also grown using substrate bias values V_b of −50, −150, and −250 V for more direct comparison to the range of conditions used in nanocomposite growth. The Ti overlayers are deposited in pure Ar at 0.5 Pa (3.75 mTorr), using a discharge power of 100 W, a target voltage of 304 V, and a floating potential $V_f = -7$ V. All bilayers are transferred to the XPS spectrometer for analysis without air exposure.

XPS spectra are recorded at take-off angles of 15°, 30°, and 90° with a Kratos AXIS Ultra instrument using monochromatic Al Kα (1486.6 eV) radiation. Binding energy scale referencing is performed using the Ar 2p line at 241.8 eV[20] for samples grown with negative bias voltages >-50 V leading to Ar incorporation during the deposition process. Spectra from all other samples are referenced to the Fermi level, 0 eV binding energy, positioned at 50% of the valence band edge maximum.[21,22] The two referencing techniques yield binding energies which agree to within 0.3 V. The spectra are background-corrected using the technique introduced by Shirley[23] and aligned at the same energy to allow for better comparison. Electron inelastic mean-free paths Λ at the kinetic energy of a Ti 2p3/2 photoelectron excited by Al K_α x-rays are very similar for the two primary overlayer materials of interest, Si (2.444 nm) and Si_3N_4 (2.457 nm).[24] Λ is somewhat lower for Ti (2.189 nm) and TiN (1.960 nm). Peak positions and their relative intensities are evaluated by fitting the experimental Ti 2p and Si 2p peaks with Gauss-Lorentz asymmetric line shapes[25] using CasaXPS.[26] All layers have oxygen concentrations $\leqslant 1$ atomic%.

Overlayer thicknesses are chosen such that in each case, the interface with TiN(001) is transparent to photoelectrons and thereby accessible for XPS analysis without sputter etching to avoid distorting the interface information due to atomic mixing. Since for Si_3N_4/TiN(001) samples, N is present in both layers, changes in the Ti 2*p* spectra are used to compare the chemistry and electronic structure of the interfaces. Si 2*p* spectra provide information regarding changes in the chemical state of Si at the surface and at the interface of Si_3N_4/TiN(001) and Si/TiN(001) samples. Depth-dependent information is obtained using AR-XPS in which spectra are acquired at 90° (along the surface normal), 30°, and 15°.

Layer compositions are determined by RBS, following XPS analyses, using a 2 MeV He^+ primary beam incident at an angle of 22.5° relative to the sample normal; the detector is set at a 150° scattering angle. Deposition rates are measured via determination of the number of deposited atoms, as measured by RBS. The total accumulated ion dose is 100 μC. Backscattered spectra are analyzed using the RUMP simulation program.[27]

III. RESULTS

A. Clean, as-deposited TiN(001)

Figure 1 shows typical angle-resolved Ti 2p photoelectron spectra (take-off angles θ = 15°, 30°, and 90°) from as-deposited TiN(001). The $2p_{3/2}$ and the $2p_{1/2}$ peaks appear at 454.9 and 461.9 eV, each with corresponding satellite peaks

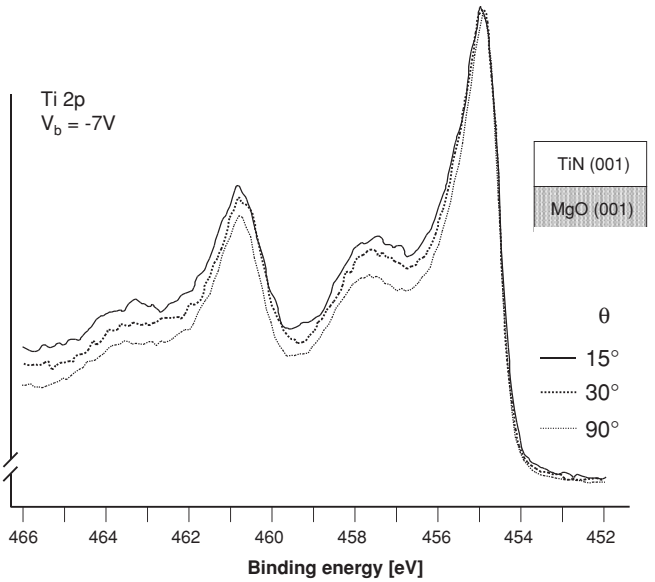

FIG. 1. *In situ* AR-XPS spectra from clean TiN(001) showing the Ti $2p_{3/2}$ (454.9 eV) and Ti $2p_{1/2}$ (460.9 eV) features from freshly deposited TiN(001) at three different electron take-off angles $\theta = 15$, 30, and 90° (orthogonal to the substrate). The corresponding shake-up satellite features, separated by ∼2.65 eV, are more intense at lower electron take-off angles.

shifted ∼2.6 eV to higher binding energies in agreement with spectra[28] for clean stoichiometric TiN(001). The satellite peaks are only observed on clean TiN and are very sensitive to the chemical environment around the Ti atoms.[28] The satellite features are intrinsic to the photoelectron line shape of clean TiN, with no distinguishable changes as a function of take-off angle, and are thus not indicative of surface oxide formation. For reference, the Ti 2p peaks for TiO_2 lie between 464.3 and 464.7 eV.[29]

Porte *et al.*[30] reported a pronounced decrease in the intensity of the satellite features in TiN_x films with decreasing x in layers with N/Ti ratios varying from 0.97 to 0.52. Moreover, when the surface of stoichiometric TiN is subjected to Ar^+ ion bombardment, as typically used for sputter etching of air-exposed samples, the intensity of the satellite peaks decreases toward zero due to preferential N removal.[28] However, the peak can be restored by bombarding the "sputter-cleaned" surface with 2.5 keV N_2^+ ions.[31] Thus, the intensity of the satellite peaks is a direct measure of the local average nitrogen concentration surrounding Ti atoms in TiN_x.

Two models have been proposed to explain the appearance of the Ti $2p$ satellite peaks. The first identifies them as final-state screening effects related to vacancy defect states,[32] while the other attributes them to plasmon loss features (collective conduction-band electron oscillation modes) giving rise to an energy loss $\hbar\omega \sim 2.6$ eV.[33,34] If the latter model were correct, we would also expect to observe higher-order satellites, shifted by $2\hbar\omega$, $3\hbar\omega$, and so on, with progressively decreasing intensity. These features are not present. Furthermore, plasmon excitations are energy-loss events extrinsic to the photoelectron emission process; that is, they occur during interaction of free photoelectrons with conduction band electrons and should be visible in N $1s$ spectra from clean stoichiometric TiN as well, which is not the case.[28] The fact that the intense satellite structure is only observed in the Ti $2p$ spectra is consistent with the assignment by Porte *et al.*[30] that the features are intrinsic to Ti $2p$ photoionization and predominantly due to core-hole screening.

Ionization of the core subshell results in a strong perturbation of the electrostatic potential responsible for producing localized states. Final-state screening occurs when electrons are transferred to localized states that screen the core hole. When the transfer occurs, the total energy of the final-state is lowered giving rise to a "screened" photoelectron feature at lower binding energy. When the transfer does not occur, the total energy of the final-state is higher, resulting in a higher binding energy "unscreened" final-state.

Porte *et al.*[30] attributes the Ti $2p_{3/2}$ and $2p_{1/2}$ peaks to the screened final state and the satellite feature to photoelectron emission from Ti with an unscreened core hole. They also report an accompanying increase in the density of states (DOS) at approximately 2 eV below the Fermi level in TiN_x valence-band spectra from a series of samples with decreasing nitrogen content. This has the effect of filling the characteristic minimum in the stoichiometric TiN DOS between the N $2p$ and the Ti $3d$ dominated bands just below the Fermi level. The additional DOS is attributed to delocalized vacancy states which form a band as the vacancy concentration on the anion sublattice increases above 20% (TiN_x with $x < 0.8$). The increased electron concentration near the Fermi level enhances the effectiveness of the screening process, thus decreasing the satellite features in photoelectron spectra from N-deficient layers. Conversely, as the number of N vacancies diminishes, the vacancy states become more localized, eliminating the vacancy band and thus limiting the degree of screening. This results in a photoemission line shape with a pronounced increase in the intensity of the unscreened final-state satellite. Thus, the intensities of the satellite features are directly related to the electron DOS in the valance band just below the Fermi level, which in turn depends on the N concentration in the film.

B. Si_3N_4 / TiN(001)

When freshly deposited epitaxial TiN(001) is covered with 4 ML of Si_3N_4 grown under floating bias conditions, both the intensity and the width of the Ti $2p$ satellite structure exhibit a marked increase (see Fig. 2). The intensity increase is even more significant at shallow takeoff angles, which primarily probe the Ti atoms at the interface.

When Si_3N_4 is deposited on TiN(001) at increased substrate bias voltages, the effects observed with floating bias conditions are enhanced. Figure 3 compares Ti $2p$ spectra, all acquired at a 15° takeoff angle, of 4 ML Si_3N_4 / TiN(001) samples grown with $V_b = -7$, -150, and -250 V. A distinct increase in the satellite intensity is observed as the bias voltage during Si_3N_4 deposition is increased. For Si_3N_4 overlayers grown with $V_b = -250$ V, the Ti satellite peak is nearly as intense as the main core level peak. We note that this cannot be due to N loss at the TiN near-surface since this would decrease the intensity.[30,31] The observed intensity change with V_b is far higher than that reported for TiN_x with variations of x.

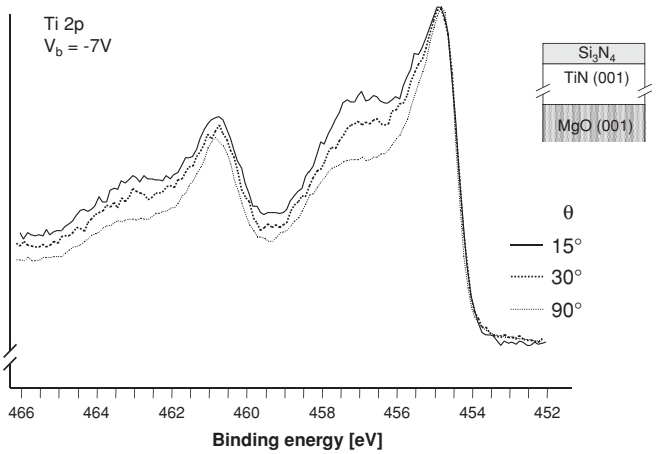

FIG. 2. *In situ* AR-XPS spectra from 4 ML Si_3N_4/TiN(001) bilayers, acquired at $\theta = 15$, 30, and 90°, showing Ti 2*p* and corresponding satellite features.

On the nonpolar TiN(001)1 × 1 surface, each Ti is surrounded by five N atoms and vice versa. The deposition of Si_3N_4 results in an increased N concentration around surface and near-surface Ti atoms, resulting in negative polarization due to the higher electronegativity of N than Ti. This effect is enhanced with increasing substrate bias V_b due to increasing irradiation with low energy N_2^+ ions. The interface chemistry with low and high V_b is illustrated schematically in Fig. 4.

The observed interfacial polarization, as evidenced by the XPS spectra, with fractionally negatively charged N and fractionally positively charged Ti, indicates that the origin of the polarization effect is the enhanced Ti coordination by N upon coverage of TiN(001) with Si_3N_4, rather than Si bonding directly to the topmost Ti atoms. The latter would lead to the formation of titanium silicides, which are reported to be necessary for obtaining ultrahardness in Ti-Si-N nanocomposites.[35] If silicides were formed at the interface, they would be observable via an increased binding energy

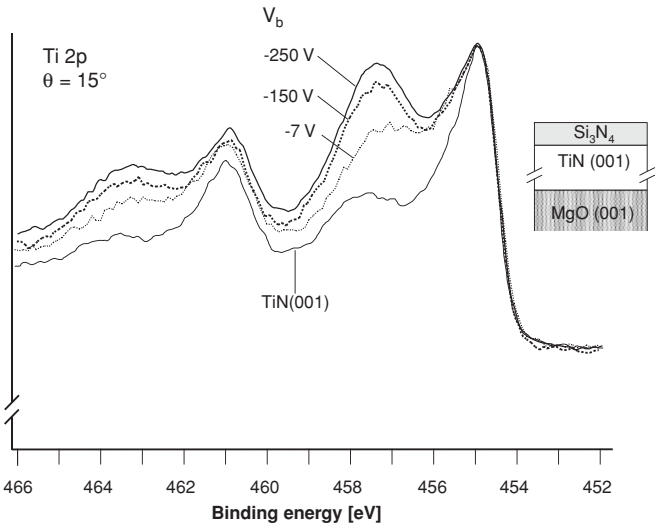

FIG. 3. *In situ AR-XPS* Ti 2*p* and corresponding satellite features from 4 ML Si_3N_4/TiN(001) bilayers, in which the Si_3N_4 layers are grown at substrate bias voltages V_b of −7, −150, and −250 V.

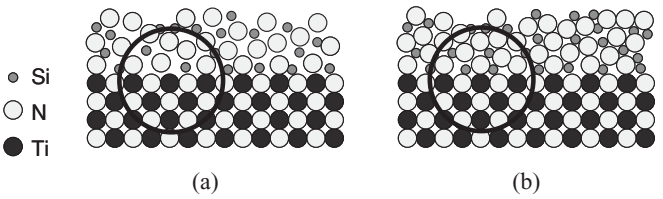

FIG. 4. Schematic view of Si_3N_4/TiN(001) interface architectures in which the Si_3N_4 layers are grown at (a) floating potential, $V_b = -7$ V, and (b) at high substrate bias, $V_b = -150$ V. The circled regions illustrate different average bond coordinations around Ti interface atoms.

difference of of 0.6 to 1.1 eV between the Ti 2*p* and the Si 2*p* peaks.[36] However, our XPS results reveal no indication of $TiSi_x$ formation for all investigated substrate bias values. The energy difference remains constant at 353.1 ± 0.1 eV. This suggests the absence of significant Ti-Si bond density at the Si_3N_4/TiN interface. However, as shown in section 4.4, Ti-Si bonds are, as expected, observed at the Si/TiN interface.

C. TiN / Si_3N_4

As a self-consistency check that we are actually probing interfacial bonding in Si_3N_4/TiN interfaces, we also grow and analyze the inverse structure (i.e., 4 ML of TiN on a thick layer of amorphous Si_3N_4). The TiN layer was deposited with a substrate bias voltage V_b of −150 V, and in contrast to the previously described experiment series, and it is polycrystalline. Since the XPS Ti 2*p* features are no longer sensitive to just the interface (we now probe the entire TiN layer thickness), the intensity of the Ti 2*p* satellite peaks should lie between the binding energies of those measured for clean TiN and those for Si_3N_4/TiN. This is indeed what is observed in the spectra shown in Fig. 5. A comparison is shown among uncoated TiN(001) (from Fig. 1), Si_3N_4/TiN(001) (from Fig. 3), and TiN/a-Si_3N_4. To obtain the maximum interface sensitivity, the latter spectrum is recorded normal to

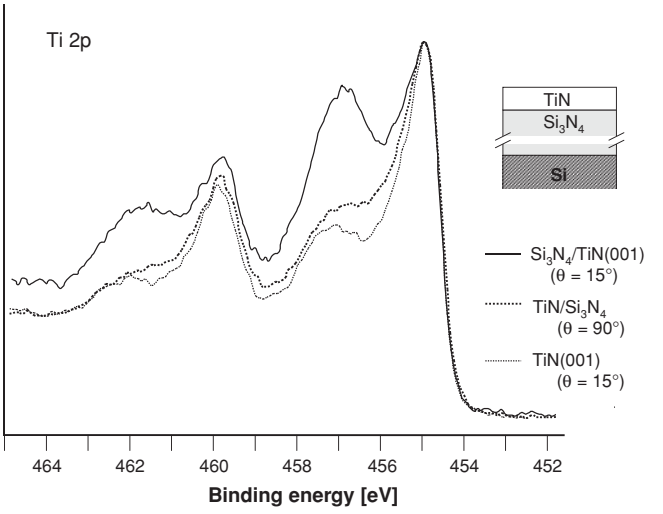

FIG. 5. Comparison of XPS Ti 2*p* spectra, obtained at $\theta = 15°$, for TiN(001), Si_3N_4/TiN(001), and TiN/a-Si_3N_4. Note that the satellite intensities for TiN/Si_3N_4 are much lower than from Si_3N_4/TiN, but higher than for clean TiN(001).

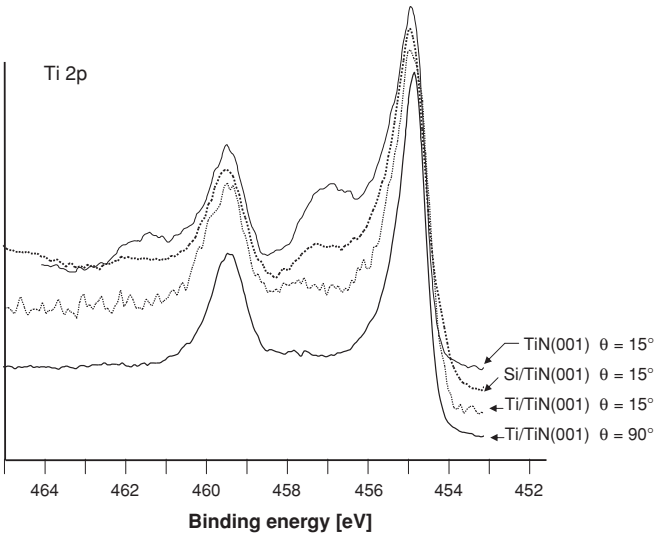

FIG. 6. *In situ* AR-XPS spectra showing the Ti 2*p* and corresponding satellite features from 4 ML Si/TiN(001) and Ti/TiN(001) bilayers. Satellite intensities are markedly reduced in comparison to clean TiN(001) due to additional interfacial valence band electrons provided by the overlayer.

the sample surface; low electron take-off angles will primarily probe the TiN surface (i.e., the interface with vacuum). These results provide further evidence that the satellite peaks monitor the average N concentration around Ti atoms. In addition, it is important to note that the spectra provide no evidence that a substrate bias of −150 V induces N deficiency.

D. Si/TiN and Ti/TiN

The degree of nitridation in TiN/Si_3N_4 nanocomposites is decisive for obtaining increased hardness. N-deficient $SiN_{1.33-x}$, which contains Si atoms in both the fully nitrided and reduced state, has fewer Si-N bonds, and hence suffers from reduced cohesion of the binder phase and the overall nanocomposite consequently has lower hardness.[4,15] Thus, a complete description of the interface in TiN/SiN_x nanocomposite should also include the interaction of Si with TiN.

XPS spectra from freshly deposited Si/TiN(001), see Fig. 6, show that the intensities of the Ti 2*p* satellites are markedly reduced with respect to pristine TiN(001). The Si 2*p* peak develops an asymmetry on the low binding energy side; the energy difference between the fitted components amounts to 0.55 eV, which is indicative of Ti-Si bonding.[36] This assignment is supported by the fact that the energy difference between the Ti 2*p* and the Si 2*p* peaks increases by ∼2.0 eV compared to the Si_3N_4/TiN(001) case, for which no $TiSi_x$ formation is detected. This implies that additional valence electrons are available to screen the Ti core electrons and thus reduce the Ti 2*p* satellite intensity. The additional valence electrons originate from nonnitrided Si atoms, which did not react to form $TiSi_x$. Peak fitting of the Si 2*p* peak shows that $TiSi_2$ accounts for approximately 60% of the total Si 2*p* peak intensity.

More electrons located in the Si valence band at the interface thus enhance the screening effect (i.e., they reduce the satellite intensity). This can also be achieved by adding electrons from a metal [e.g. by depositing metallic Ti on TiN(001)]. Indeed, XPS results show that the deposition of 4 ML of Ti leads to an almost complete loss of the satellite structure. Note, however, that the N1*s* peak is still present, which means that either the 4 ML Ti layer is partially transparent to N1*s* photoelectrons, or the Ti layer is rough and discontinuous. The angular dependence of the N1*s* intensity shows that the Ti layer is continuous and relatively smooth. The spectrum obtained at a take-off angle of 90° probes the Ti/TiN interface more effectively due to the higher sampling depth. Nevertheless, the Ti 2*p* peak is not specific to the interface, as is the case for Si/TiN(001); it is composed of contributions from both the Ti overlayer and the TiN underlayer. Subsequent exposure of the Ti overlayer to nitridation at a N_2 pressure of 10^{-4} Pa ($7.5 \cdot 10^{-4}$ mTorr) at 640 °C for 1 h completely restores the TiN spectrum with a satellite intensity equal to that observed on single-crystalline TiN(001). This series of experiments further illustrates that changes in the electron density in the valence band modify screening of core level Ti 2p holes, and in this way determine the intensity of the satellite peak.

IV. DISCUSSION

The experiments described here clearly show that changes in the valence electron density at Si_3N_4/TiN(001), Si/TiN(001), Ti/TiN(001), and TiN/a-Si_3N_4 interfaces can be monitored using the satellite peak intensity. Interfacial charge accumulation in the case of Si_3N_4/TiN(001) or charge depletion for Si/TiN(001) and Ti/TiN(001), as evidenced by the corresponding changes in the measured satellite intensities, is linked to the electronic structure of the overlayer material. Interfacial charge accumulation is strongest for materials with a high band gap E_g (E_g for bulk β-Si_3N_4 is 5.25 eV[37]), while that of a-Si_3N_4 is 4.9 eV,[38] as the Si_3N_4/TiN(001) experiments show. The satellite intensity is dramatically reduced with Si ($E_g = 1.1$ eV) overlayers and essentially eliminated with Ti ($E_g = 0$ eV) overlayers. This is consistent with the results shown in Fig. 3, comparing XPS spectra from Si_3N_4/TiN(001) overlayers grown with increasing V_b, suggesting that enhanced interfacial bonding is obtained at higher bias values. For comparison, TiN/Si_3N_4 nanocomposites deposited without substrate bias suffer from insufficient adatom mobility, leading to columnar open structures.[39] Increasing the substrate bias leads to enhanced adatom mobility, dense coatings, and increased hardness,[4,39] Thus, our results suggest that increased interfacial N is linked to higher hardness.

Contact between dissimilar materials requires Fermi level alignment. The Fermi level of a metal corresponds to the highest occupied level, while for an insulator it is located in the middle of the band gap. Formation of the Si_3N_4/TiN interface therefore results initially in an energy difference between the highest occupied TiN and Si_3N_4 levels of approximately half the Si_3N_4 band gap (i.e., 2.5 eV). There is no significant band bending in the 4 ML Si_3N_4 layer.[40,41] At the interface, electrons flow from the valence band of TiN to the overlayer material Si_3N_4; in this way an electrostatic polarization is introduced which strengthens the Si_3N_4/TiN(001) interface. Fig. 7(a) is a schematic drawing of the interfacial band structure of Si_3N_4/TiN(001), Si/TiN(001), and Ti/TiN(001)

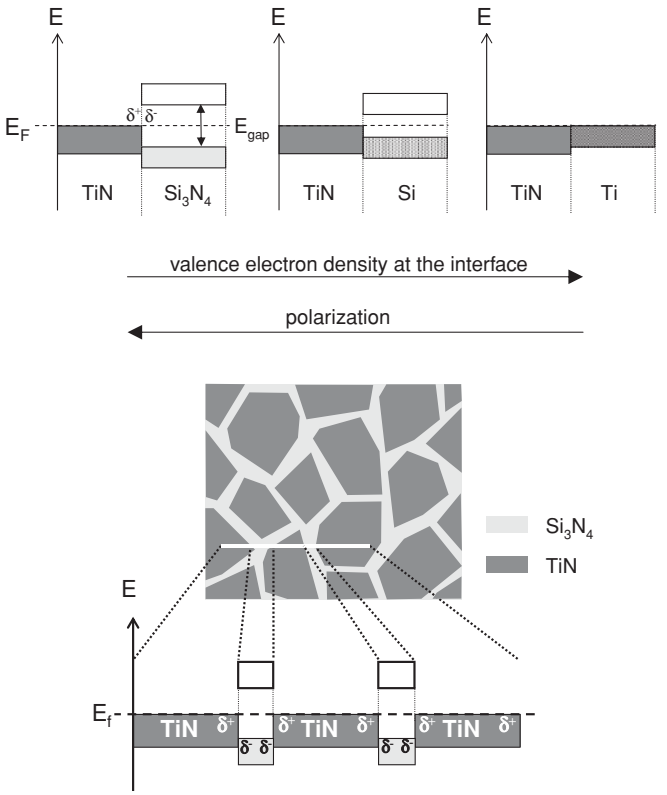

FIG. 7. (a) Schematic illustrations of the interfacial valence band structure of 4 ML Si_3N_4/TiN(001), Si/TiN(001), and Ti/TiN(001) bilayers. (b) Schematic illustration of the interfacial band structure, illustrating polarization at TiN/Si_3N_4 nanocomposite boundaries.

heterostructures. An increasing overlayer bandgap implies a larger number of free electrons available to populate the interface valence band, and thus enhanced polarization. A schematic translation of this result to a three-dimensional nanocomposite is illustrated in Fig. 7(b) for a TiN-Si_3N_4 nanocomposite. Polarization bond strengthening increases with the interface area per unit volume (i.e., with smaller crystallite size). This interface strengthening mechanism, based on our angle-resolved XPS results, is consistent with data showing that the hardness of nanocomposites increases with decreasing crystallite size.[42]

Conversely, when the contacting overlayer has a smaller band gap, or none at all (a metal), electrons are donated by the overlayer to TiN, thus decreasing the interfacial polarization and hence the interface strength as observed in N-deficient TiN/SiN_x nanocomposites, for which the tissue phase contains elemental Si.

An estimate of the overlayer band gap, at which polarization-induced interface strengthening becomes significant, is obtained by plotting the ratio of the satellite intensity to that of the Ti $2p_{3/2}$ peak, $I_{sat}/I_{Ti2p3/2}$, versus the band gap of the overlayer material, as shown in Fig. 8. For overlayer materials exhibiting intensity ratios less than that for TiN itself (i.e., ~0.85) reduced or no polarization should occur and, hence, no electrostatic enhancement of the interface strength can be expected. Lowering the N content in Si_3N_4 (i.e., increasing the fraction of elemental Si in $SiN_{1.33-x}$) is equivalent to approaching the situation with only interfacial Si instead of

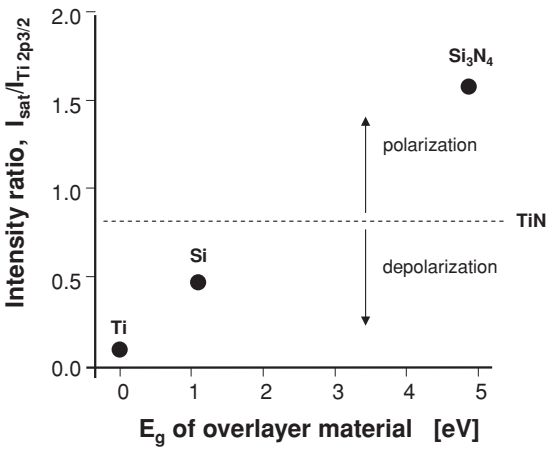

FIG. 8. Measured ratios of the satellite to Ti2p3/2 peak intensities, $I_{sat}/I_{Ti2p3/2}$, for 4 ML Si_3N_4/TiN(001), Si/TiN(001), and Ti/TiN(001) bilayers plotted versus the bulk overlayer band gap E_g.

interfacial Si_3N_4. This provides an explanation of why the presence of elemental interfacial Si lowers the hardness of TiN/Si_3N_4 nanocomposites. In fact, a hardness enhancement, referenced to that of pure TiN (~23 GPa[43]) to values of about 35 GPa was reported for nc-TiN/SiN_x with $x = 1.25$ (at about 15 mole% SiN_x), whereas a nanocomposite with $x = 0.95$ did not show such an enhancement.[15]

Density functional theory (DFT) calculations of the interfacial structures of TiN(111)/Si_3N_4/TiN(111) trilayers were carried out by Hao *et al.*[44] in which one and two ML of ordered crystalline Si_3N_4 are inserted between TiN(111) slabs. Their results show that the Si atoms intercalated between the nitrogen-terminated TiN(111) have a more negative environment than in β-Si_3N_4.[44] Similarly, Zhang *et al.* calculated charge distributions in TiN/fcc-SiN/TiN (111) slabs[45] and found that charge transfer occurs from Ti-N interface bonds to N in SiN_x. This is consistent with the present AR-XPS spectroscopic data from 4 ML Si_3N_4/TiN(001) bilayers Both results show that increasing interfacial polarization, together with other parameters such as crystallite size and tissue layer thickness, is expected to lead to higher hardness in nanocomposite materials.

V. CONCLUSIONS

The deposition of several monolayers of Si_3N_4, Si, and Ti on single-crystalline TiN(001) has a pronounced influence on the intensities of the Ti 2p photoelectron satellite peaks. Using *in situ* AR-XPS, we show that this effect is very sensitive to the electronic structure of the interface between TiN and the overlayer. The satellite intensity is a direct measure of the interface valence electron density, which is, in turn, directly related to the interfacial bond strength. Deposition of Si_3N_4 on TiN(001) results in the formation of a N-rich interlayer which accepts free electrons that screen titanium atoms at the interface. Consequently, a polarization of the interface develops. The effect is further enhanced by the application of a negative substrate bias voltage during Si_3N_4 reactive deposition in mixed Ar/N_2 discharges. In contrast, overlayers of Si, and even more so, of Ti, donate electrons to the TiN valence band. The observed polarization of the Si_3N_4/TiN

interface enhances interfacial strength and provides an explanation of enhanced hardness in TiN/Si_3N_4 nanocomposite coatings deposited under conditions of full nitridation of the $SiN_{1.33-x}$ phase ($x = 0$). Insufficient nitridation ($x > 0$) results in an increasing contribution of Si atoms in contact with TiN, and hence a weakened interface.

ACKNOWLEDGMENTS

This research was carried out, in part, in the Frederick Seitz Materials Research Laboratory Central Facilities, University of Illinois, which are partially supported by the US Department of Energy under Grants No. DE-FG02-07ER46453 and No. DE-FG02-07ER46471.

*joerg.patscheider@empa.ch

[1] S. Vepřek, M.G.J. Veprek-Heijman, P. Karvankova, and J. Prochazka, Thin Solid Films **476**, 1 (2005).

[2] S. Vepřek, J. Vac. Sci. Technol. A **17**, 2401 (1999).

[3] S. Vepřek and S. Reiprich, Thin Solid Films **268**, 64 (1995).

[4] M. Diserens, J. Patscheider, and F. Levy, Surf. Coat. Technol. **120-121**, 158 (1999).

[5] F. Vaz, L. Rebouta, S. Ramos, M. F. da Silva, and J.C. Soares, Surf. Coat. Technol. **108–109**, 236 (1998).

[6] P. Jedrzejowski, J. E. Klemberg-Sapieha, and L. Martinu, Thin Solid Films **426**, 150 (2003).

[7] J. S. Colligon, V. Vishnyakov, R. Valizadeh, S. E. Donnelly, and S. Kumashiro, Thin Solid Films **485**, 148 (2005).

[8] A. Flink, T. Larsson, J. Sjölén L. Karlsson, and L. Hultman, Surf. Coat. Technol. **200**, 1 (2005).

[9] P. Rogl and J. C. Schuster, *Phase Diagrams of Ternary Boron Nitride and Silicon Nitride Systems* (ASM International, Materials Park, OH, 1992).

[10] H. Söderberg, M. Odén, J. M. Molina-Aldareguia, and L. Hultman, J. Appl. Phys. **97**, 114327 (2005).

[11] J. Schiøtz and K. W. Jacobsen, Science **301**, 1357 (2003).

[12] A. Hasnaoui, H. Van Swygenhoven, and P. M. Derlet, Science **300**, 1550 (2003); H. van Swygenhoven, *ibid.* **296**, 66 (2002).

[13] P. Nesladek and S. Vepřek, Phys. Stat. Sol. (a) **177**, 53 (2000).

[14] S. Vepřek, A. S. Argon, and R. F. Zhang, Phil. Mag. Lett. **87**, 955 (2007).

[15] F.-J. Haug, P. Schwaller, F. Wloka, J. Patscheider, A. Karimi, and M. Tobler, J. Vac. Sci. Technol. A **22/4**, 1229 (2004).

[16] T. Serikawa and A. Okamoto, Thin Solid Films **101**, 1 (1983).

[17] L. Hultman, J. Bareño, A. Flink, H. Söderberg, K. Larsson, V. Petrova, M. Odén, J. E. Greene, and I. Petrov, Phys. Rev. B **75**, 155437 (2007).

[18] C.-S. Shin, S. Rudenja, D. Gall, N. Hellgren, T.-Y. Lee, I. Petrov, and J. E. Greene, J. Appl. Phys. **95**, 356 (2004).

[19] R. C. Powell, N.-E. Lee, Y.-W. Kim, and J. E. Greene, J. Appl. Phys. **73**, 189 (1983).

[20] J. F. Moulder, W. F. Stickle, P. E. Sobol, and K. D. Bomben, *Handbook of Photoelectron Spectroscopy*, edited by J. Chastain, R. C. King Jr. (Physical Electronics, Eden Prairie, MN, 1995).

[21] S. Hüfner, *Photoelectron Spectroscopy Principles and Applications*, 2nd ed. (Springer, Heidelberg, 1995), p. 7.

[22] D. Briggs and J. C. Rivière, *Practical Surface Analysis,* 2nd ed., Vol. 1, edited by D. Briggs and M. P. Seah (John Wiley and Sons, Chichester, England, 1983), p. 116.

[23] D. A. Shirley, Phys. Rev. **55**, 4709 (1972).

[24] S. Tanuma, C. J. Powell, and D. R. Penn, Surf. Interf. Anal. **21**, 165 (1994); [http://www.quases.com/QUASES_IMFP_TPP2M/QUASES_IMFP_TPP2_home.htm].

[25] G.K. Wertheim, J. Electron Spectrosc. **6**, 239 (1975).

[26] [http://www.casaxps.com].

[27] L. R. Doolittle, Nucl. Instrum. Methods Phys. Res. B **15**, 227 (1985).

[28] R. T. Haasch, T.-Y. Lee, D. Gall, C.-S. Shin, J. E. Greene, and I. Petrov, Surf. Sci. Spectra **7**, 193 (2000).

[29] NIST XPS database: [http://srdata.nist.gov/xps/].

[30] L. Porte, L Roux, and J Hanus, Phys. Rev. B **28**, 3214 (1983).

[31] I. Bertóti, Surf. Coat. Technol. **151-152**, 194 (2002).

[32] L. I. Johansson, Surf. Sci. Rep. **21**, 177 (1995).

[33] S. Logothetidis, E. I. Meletis, and G. Kourouklis, J. Mater. Res. **14/2**, 436 (1999).

[34] B. D. Ratner and D. G. Castner, in *Surface Analysis*, edited by J. Vickerman (J. Wiley & Sons, Chichester, England, 1997), p. 43.

[35] S. A. Niederhofer, P. Nesladek, H.-D. Männling, K. Moto, S. Vepřek, and M. Jilek, Surf. Coat. Technol. **120–121**, 173 (1999).

[36] S. A. Chambers, D. M. Hill, F. Xu, and J. H. Weaver, Phys. Rev. B **35**, 634 (1987).

[37] Y.-N. Xu and W. Y. Ching, Phys. Rev. B **51**, 17379 (1995).

[38] T. Hashizume, S. Ootomo, T. Inagaki, and H. Hasegawa, J. Vac. Sci. Technol. B. **21**, 1828 (2003).

[39] F. Vaz, L. Rebouta, Ph. Goudeau, T. Girardeau, J. Pacaud, J. P. Rivière, and A. Traverse, Surf. Coat. Technol. **146–147**, 274 (2001).

[40] G. Lihui, Z. Yibin, and S. Tietun, Sol. Energ. Mat. Sol. C. **43**, 325 (1996).

[41] S. A. Chevtchenko, M. A. Reshchikov, Q. Fan, X. Ni, Y. T. Moon, A. A. Baski, and H. Morkoç, J. Appl. Phys. **101**, 113709 (2007).

[42] S. Vepřek, Thin Solid Films **317**, 449 (1998).

[43] B. O. Johansson, J.-E. Sundgren, and J. E. Greene, J. Vac. Sci. Technol. **3**, 303 (1985).

[44] S. Hao, B. Delley, and C. Stampfl, Phys. Rev. B **74**, 035402 (2006).

[45] R. F. Zhang, A. S. Argon, and S. Vepřek, Phys. Rev. B **81**, 245418 (2010).